Journal of The Electrochemical Society, **155** (12) F253-F265 (2008)
0013-4651/2008/155(12)/F253/13/$23.00 © The Electrochemical Society

Relation Between Morphology, Etch Rate, Surface Wetting, and Electrochemical Characteristics for Micromachined Silicon Subject to Galvanic Corrosion

David C. Miller,[z] **Collin R. Becker, and Conrad R. Stoldt**

Department of Mechanical Engineering, and DARPA Center for Integrated Micro/Nano-Electromechanical Transducers (iMINT), University of Colorado, Boulder, Colorado 80309, USA

Immersion of silicon in HF-based solutions is utilized in microsystems fabrication to render freestanding mechanical structures. Such etching, however, creates a galvanic couple between silicon and a metallic layer (e.g., gold), resulting in corrosion damage. Morphology, resistive probe, surface wetting, and electrochemical characterization (vs Cu/CuF) of single- and polycrystalline silicon subjected to galvanic corrosion in three HF-based solutions (undiluted 48% HF, UDHF:H_2O, and UDHF:Triton X-100) are used here to formally substantiate the results of a previous mechanical (microtensile) study. Porosity estimated from the morphology of corroded samples allows the corrosion current density to be determined from etch-rate measurements, according to Faraday's law. Resistive probe structures are used to simulate the microtensile specimens, thereby characterizing corrosion current as a function of time, etchant type, illumination, and the amount of metal utilized. The measured current density of micromachined silicon is compared against (100) wafer specimens using polarization characterization, identifying the porous Si formation regime. Using sessile drop measurements, the three etchants are further distinguished based on their surface-wetting characteristics. The chronopotentiometry, resistive probe, and microtensile characterizations all identify the behavior regimes of rapid initiation, subsequent steady-state corrosion, and the final catastrophic failure of the microtensile specimens.

© 2008 The Electrochemical Society. [DOI: 10.1149/1.2996249] All rights reserved.

Manuscript submitted May 5, 2008; revised manuscript received September 8, 2008. Published October 24, 2008.

Galvanic corrosion has become a growing concern in the field of microelectromechanical systems (MEMS). Many microfabricated components are comprised of multiple material layers; and, in particular, metallic layers may be added to Si structural layers to enable electrical, optical, or chemical applications.[1] In all cases, the constituent materials (e.g., Au and Si) are typically in electrical contact and exist at inherently different electrochemical potentials. As a consequence, a galvanic cell is created upon immersion in the HF-based solutions[2-7] commonly used during the dissolution of sacrificial SiO_2 interlayers. On the basis of the potential difference, the oxidation of Si is thermodynamically favored, i.e., Au acts as the cathode and Si acts as the anode.[3-7] The autonomous corrosion of Si in HF may occur according to a porous silicon (PS) formation process,[2-7] similar to the condition where an externally applied electric signal is used to intentionally generate PS.[8-11] Others have suggested that electropolishing (EP) may occur at the Si surface.[5] Corrosion-induced damage has been shown to limit or compromise MEMS performance and reliability by degrading mechanical characteristics, including modulus,[1,12] strength,[1,13] hardness,[12] and fatigue life[5] for miniaturized polycrystalline silicon (polySi)[1,12-14] and single-crystal silicon (SCS)[1,5] structures. In particular, the damage morphology and corresponding mechanical performance has been found to correlate with the etchant solution utilized (i.e., microstructure specific vs generalized attack), which was suggested to relate to the surface wetting characteristics present during corrosion.[1]

The resistive probe is a technique commonly used to monitor or predict corrosion.[15] In this technique, measured electrical resistance is related to the physical loss of material. Certain assumptions allow the resistive probe technique to be applied to the study of galvanic corrosion in MEMS components. For example, the surface material remaining after corrosion is considered nonconductive as dopant is typically depleted during PS formation or EP, resulting in an increase in resistance as great as 5 orders of magnitude.[8-11,16] The motivation to monitor Si corrosion using a resistive probe is based on the increased electrical resistance reported in the literature.[12,17] In each study, greatly increased resistance was observed for micromachined polySi etched in undiluted 48 wt % HF (UDHF).

Through a fundamental analysis, damaged Si structures (e.g., resistive probes) can be compared against electrochemical characterization. If the rate of corrosion is known, then the corrosion current density may be determined according to Faraday's law (Eq. 1).[15] Another variant of Faraday's law may be used to calculate the thickness of the affected Si (Eq. 2). In Eq. 1 and 2, the parameter j represents the electrical current density ($\mathrm{C/s{\cdot}m^2}$), ρ the density of intact Si (in grams per cubic meter), λ the net valence of the reaction sequence (unitless), r the rate of corrosion (in meters per second), F Faraday's constant 96,485.338 (C/mol), P the porosity of the remaining surface layer, M_m the molar mass of Si (in grams per molecule), t_c the thickness of the affected Si (in meters), Q the total electrical charge transferred (C), and A the area of anode surface (in meters squared). The net valence for Si in HF is known to be 2 for PS generation, and 4 for EP.[11] In Eq. 1 and 2, the term P is specific to PS generation, where a porous corroded surface layer will remain after HF immersion

$$j = \frac{\rho\lambda rFP}{M_\mathrm{m}} \qquad [1]$$

$$t_c = \frac{QM_\mathrm{m}}{\rho\lambda AFP} \qquad [2]$$

Besides the resistive probe technique, electrochemical characterization may be used to examine the behavior of a material system (Si and Au) and to also generalize the results to many other material combinations (Si and a metal). In the literature, several groups have examined key parameters related to the galvanic corrosion of Si, such as the open-circuit potential (OCP) of Si and Au, the mixed-pair potential, and the operant corrosion current density.[2-7] The OCP values between −0.109 and −0.23 volts relative to the saturated calomel electrode potential (V_SCE) for Si in UDHF,[5,7] and OCP values between 0.474 and 0.65 V_SCE for Au in UDHF[5,6] are reported. Actual corrosion, however, depends on the mixed-pair potential at the equilibrium state, for which an increase between 0.12 and 0.2 V above the OCP of Si has been observed.[6,7] Values for the quiescent current density of Si wafer specimens partially coated with Au and immersed in UDHF are reported to range between 0.08 and 0.64 (in microamperes per centimeters squared).[2,7] In comparison, the externally applied current density used to generate PS typically ranges from 0 to 100 (in microamperes per centimeters squared),[9,11] but can approach 250.[8,9]

Other factors examined using electrochemical characterization include the use of different metals, oxidizing agents, surfactants, and illumination.[2,3,6] For example, use of Pt instead of Au resulted in a greater mixed-pair potential. Likewise, the incorporation of hydro-

---

[z] E-mail: dcm@colorado.edu

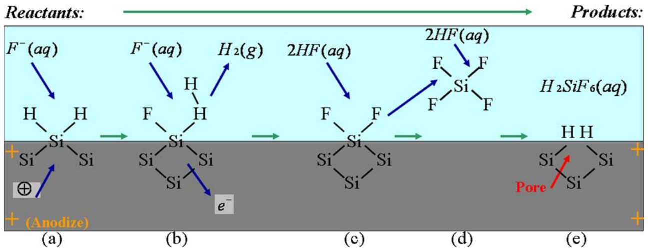

Figure 1. (Color online) Schematic representing key physiochemical events occurring at the active etch front of Si, when it is anodized in HF to generate PS.

gen peroxide (H_2O_2, a stronger oxidizing agent) increased the equilibrium potential for a mixed-pair, promoting corrosion. Alternately, the anodization current and etch uniformity were increased by using a surfactant (e.g., ethanol or Triton-X-100).[2,3] Lastly, corrosion current may be limited (or even terminated) based on the amount of light present, particularly for less doped n-type Si.[9,18] The importance of illumination was found to specifically apply to the Si dissolution process for microelectronics specific Si specimens.[2,3]

In addition to electrochemical characterization, the specific reaction chemistry sequence importantly identifies the connection between surface wetting and consumption of Si in HF. The sequence proposed by Lehmann and Gösele,[19] shown in Fig. 1, summarizes the conventional understanding of the PS formation process. The surface-bound oxidation scheme begins with the reactants Si and HF, where the Si bears an electronic (galvanic) bias as indicated with the plus symbol. In order to dissolve n-type Si, the material must be anodically (positively) biased, rendering it electron deficient. An added hole makes Si vulnerable to the fluoride ion, particularly at microstructural defects or morphological features, which then becomes adsorbed on the surface (Fig. 1a). For example, external illumination is often utilized during anodization to liberate additional electron/hole pairs by severing Si covalent bonds.[11] The adsorption of a second fluoride ion generates hydrogen gas and induces the transfer of an electron into the substrate (Fig. 1b). At this point, the Si–F surface bond is highly polar, rendering the surface vulnerable to the second fluoride ion. The net valence, λ, for the reaction sequence is 2, as defined by the loss of a hole and addition of an electron. The reaction with HF molecules generates a silicon tetrafluoride molecule, thereby removing a Si atom from the surface (Fig. 1c). In this step, the Si–F termination enables dissolution by weakening the electron density for the Si atoms, and making them vulnerable to HF. Additional HF molecules are consumed in solution when the silicon tetrafluoride is converted to hexafluorosilicic acid (Fig. 1d). The final products of the reaction sequence are a pore at the active etch front and the hexafluorosilicic acid, dissolved in solution (Fig. 1e). The surface pore will concentrate electric charge, locally rendering Si more vulnerable to continued corrosion. Corrosion typically proceeds until the Si matrix becomes dopant depleted (via tunneling through the space charge layer for degenerately doped Si or alternately through quantum confinement of carriers in less doped material).[19] The surface chemistry in Fig. 1e indicates that Si and PS typically exist in HF with the hydrophobic but organophilic hydrogen surface termination.[9,20] Figure 1 importantly illustrates the significance of the wetting characteristics, as interaction with the aqueous solution is readily influenced by the surface termination that bears at least three separate hydrophobic configurations. Furthermore, unless mechanical agitation or a surfactant is utilized, hydrogen bubbles generated in Fig. 1b will adhere to the surface,[8] preventing further chemical activity. In summary, the conventionally understood physiochemical reaction sequence indicates that surface wetting may greatly limit the process of Si dissolution, based on the hydrophobic surface species or residual by-products present.

The present study examines the corrosion of silicon on insulator (SOI), and polySi specimens subject to corrosion in HF-based solutions. The goal of this project is to determine the relationship between damage morphology (quantified via electron microscopy and the resistive probe technique), the surface-wetting characteristics of the etchant solutions utilized (specifically measured using the sessile drop technique), and the measured electrochemical response. In particular, this study is conducted to conclusively validate prior examination of the mechanical performance of SOI and polySi microtensile specimens.[1] In that study, mechanical and microstructural characterization suggested the surface wetting characteristics of the etchant utilized could greatly affect the performance and corresponding morphology of failed micromachined Si structures. Therefore, the study described here uniquely examines wafer specimens as well as micromachined structures composed of the same micromachined Si and provides comparison to single crystalline Si typical to the field of PS formation. Trends identified in the microtensile study, such as mode of material consumption (i.e., microstructure specific vs generalized attack), will be shown here to generally apply. To this end, the present study examines important considerations ("processing parameters") regarding corrosion including poly- vs single-crystalline Si, etch time, use of illumination, etchant chemistry, and the amount (surface area) of metal utilized.

Experimental

Specimens and specimen preparation.— The resistive probes consist of four-point "Van der Pauw" structures fabricated via the SOIMUMPs[21] or polyMUMPs technologies.[22] The SOIMUMPs fabrication run 14 (10 μm thick patterned Si) and polyMUMPs fabrication run 75 were utilized to create the resistive probes. The fabrication technologies are described further in Ref. 23, with the solution-based postprocessing used here being more thoroughly described in Ref. 1. Briefly, the test structures consisted of resistors in the shape of a Greek cross[24] and may be used to accurately measure electrical resistance (or resistivity).[25] Although the interconnects for the resistive probe structures were physically anchored to the substrate, the 10 μm × 10 μm active test region was typically not (i.e., it was free to corrode on all four surfaces). Cross-sectional examination of the corroded SOI, however, suggested that the layer would predominantly corrode on its top surface.[1]

For electrochemical characterization, wafers from the SOIMUMPs fabrication run 17 (10 μm thick Si) and polyMUMPs fabrication run 75 were obtained directly from the commercial vendor (MEMSCAP, Inc.). The wafers were processed according to the standard manufacturing procedure, including the thermal anneal utilized (1 h at 1050°C) to diffuse dopant into the SOI, Poly-0, or Poly-1 layers from the overlying phosphosilicate glass (PSG) layer. The resistivity of the SOI, Poly-0, and Poly-1 layers was previously found to be $4.9 \times 10^{-3} \pm 1.0 \times 10^{-4}$, $1.5 \times 10^{-3} \pm 6.0 \times 10^{-5}$, and $2.5 \times 10^{-3} \pm 5.5 \times 10^{-5}$ Ω cm, respectively.[23] As a reference to compare to the PS literature, (100) oriented, phosphorus-doped SCS wafers with the confirmed resistivity of 0.015 ± 0.003 Ω cm were obtained from The Polishing Corporation of America, Inc. All wafers were commercially diced (Micro Dicing Technology, Inc.) into 2 cm × 2 cm squares, for use with a custom electrochemical characterization fixture.

The etchant solutions used to remove the sacrificial SiO_2 layers (e.g., PSG) consisted of (a) 48 wt % HF in water (UDHF, pH 0.86), (b) 1:1 (UDHF:H_2O, pH–1.02) by volume, or (c) 20:1 UDHF:Triton-X-100 by volume. The latter solution corresponded to a concentration of 7.8×10^{-5} mol/cm^3, which was greater than the critical micelle concentration of 2.4×10^{-7} mol/cm^3 for the nonionic detergent.[26] UDHF was chosen to represent the greatest concentration available in semiconductor grade (0.027 mol/cm^3), and the latter two solutions were expected to alter the corrosion process (while added H_2O would halve the SiO_2 etch rate), based on their polar nature or improved wetting characteristics, respectively.

Measurement methods and data reduction.— A Helios Nanolab focused ion beam (FIB) machine was used to examine the surface morphology and thickness of corroded SOI and polySi specimens. The FIB was used to prepare the samples by etching a rectangular trench, several micrometers in length, width, and depth. Prior to etching, the top surface of the specimens was protected by first depositing carbon, followed by platinum masks. Cross sections were milled using the FIB machine's gallium beam at rapid (high current) and then slow (low current) material removal rates. Because it was not possible to definitively ascertain the thickness of the corroded surface layer using secondary- or backscattered-electron imaging, a proprietary trifluoroacetic acid based chemical etchant (Colonial Metals, Inc.) containing Trifluoroacetamide was used to selectively remove the corroded surface layer, thereby creating a measurable residual cavity. Porosity was determined from surface morphology images according to a manual count of the point fraction, using a transparent 5 × 5 grid.[27]

For the resistive probe structures, electrical measurements were performed using two HP 34401A multimeters (Agilent Technologies, Inc.) to separately monitor the current and voltage supplied using a HP E3661A power supply (Agilent Technologies, Inc.). The SOIMUMPs and polyMUMPs fabricated structures were characterized at the user-specified current of 1 and 3 mA, respectively, based on the stabilized resistance measurements for uncorroded specimens. The user-specified settings circumvent the limitation of equipment resolution at low currents as well as adverse self-heating effects at high currents. A Micro-Manipulator 4000 probe station (Micromanipulator Co.) was used to achieve electrical contact to the resistive probe specimens at the patterned Au.

The results from the resistance measurements were converted to an etch rate according to the following procedure: First, the original cross-sectional area was related to the final (corroded) cross-sectional area using Eq. 3, in which it was assumed that: (*i*) the resistivity of the uncorroded interior remained constant ($\rho_o = \rho_f$), (*ii*) the structure changed only in its cross-sectional area ($L_o = L_f$), (*iii*) corrosion was relatively uniform (no pitting or heterogeneous corrosion), and (*iv*) the corroded surface layer was of infinite resistivity. Second, Eq. 3 was related to the geometry specific for the Si layer using Eq. 4 and 5, or 6, which represented the final cross-sectional area, A_f, and implied a uniform corrosion rate at the active surface(s). Equations 4-6 considered the following number of active surfaces: 1 (SOI corrodes on the top surface only in Eq. 4), 3 (the top and two side surfaces of Poly-0 in Eq. 5—the bottom surface was adhered to the substrate), or 4 (the top, bottom, and two side surfaces of Poly-1 in Eq. 6)

$$\frac{R_o A_o}{\rho_o L_o} = \frac{R_f A_f}{\rho_f L_f} \Rightarrow A_f = \frac{R_o A_o}{R_f} \qquad [3]$$

$$A_f = (b_o)(t_o - t_c) \qquad [4]$$

$$A_f = (b_o - 2t_c)(t_o - t_c) \qquad [5]$$

$$A_f = (b_o - 2t_c)(t_o - 2t_c) \qquad [6]$$

Third, the rate of corrosion was calculated from the ratio of the thickness of the corroded surface layer, t_c (in meters), to the time elapsed during etching, t (in seconds). In the equations, the parameter R refers to the electrical resistance in ohms, A the cross-sectional area of the test (gauge) section (in meters squared), ρ the resistivity in ohms per meter, L the length of the gauge (in meters), b the width of the gauge (in meters), t the gauge thickness (in meters), and r the etch rate (in meters per second). The subscripts o and f refer to the gauge's original, and final condition, respectively.

The contact angle was measured for the HF-based solutions according to the sessile drop technique.[28] Specifically, 10 μL of solution was dispersed and then imaged in profile using a digital microscope. The contact angle was examined for two types of silicon specimens: (*i*) specimens immersed in HF for 1 min and then immediately analyzed or (*ii*) specimens anodized at a prior time at the specified current density of 25 (in microamperes per centimeters squared) for 10 min. The sessile drop measurements may be analyzed according to Eq. 7, which considers the equilibrium of in-plane "forces" about a point at the interface between the liquid (etchant), solid (Si), and vapor (ambient atmosphere) present. Within laboratory conditions, γ_{sv} is usually significantly greater than γ_{sl}, motivating the liquid to spread onto the solid, thereby reducing its free energy. Equation 8 expresses the work of adhesion, which quantifies the reversible work of separating the liquid and solid phases. In the equations, θ represents the contact angle (in degrees), and W the work of adhesion (in Joules per meter squared). The subscripts lv, sv, and sl refer to the liquid-vapor, solid-vapor, and solid-liquid interfaces, respectively. For a liquid, γ the surface energy (in Joules per meter squared) is equal to its surface stress, which may be evaluated per unit width (in Newtons per meter)[29]

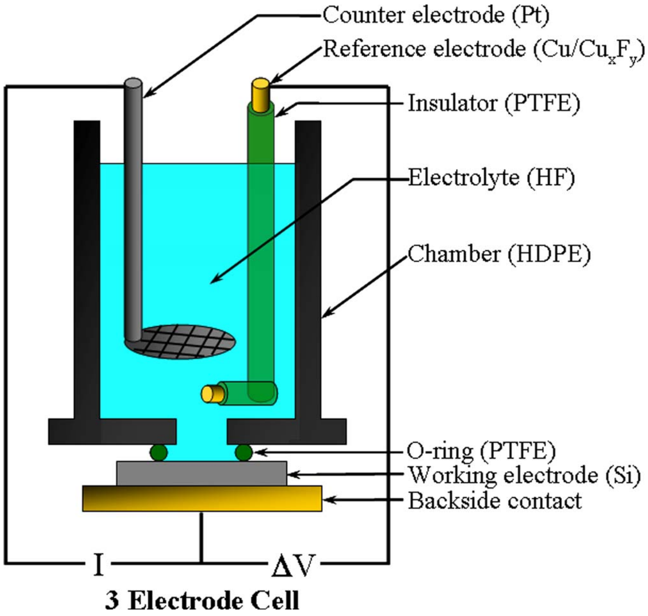

Figure 2. (Color online) Schematic showing cross-sectional view of the custom three-electrode fixture used for electrochemical characterization.

$$\gamma_{lv} \cos\theta = \gamma_{sv} - \gamma_{sl} \qquad [7]$$

$$W_a = \gamma_{lv}(1 + \cos\theta) \qquad [8]$$

Electrochemical characterization was performed using an Epsilon-E2 potentiostat/galvanostat (Bioanalytical Systems, Inc.) connected to a custom fixture (Fig. 2). The Epsilon-E2 has a 0.1 mV resolution and a 30 pA leakage current specification for the ranges utilized in most characterizations. In a few cases, a PWR-3 amplifier (Bioanalytical Systems, Inc.) was used to increase the maximum current capability from 10 to 1 A. In the experiments, the working electrode was Si, the counter electrode was Pt, and the reference electrode was Cu/CuF. For each test, 25 mL of fresh HF-based solution was contained within a high-density-polyethylene (HDPE) chamber (Fig. 2). The chamber was sealed to the Si specimen using a polytetrafluoroethylene (PTFE, Teflon) o-ring, to isolate a circular test area. To promote mechanical robustness and efficient exchange of specimens, the die was pressed upward against the HDPE chamber using a stainless steel plate, rather than using polymer-based mechanical threading.[8,9] After a 1 min dip in UDHF to remove any native oxide, the die was contacted to the plate using colloidal silver paint (Electron Microscopy Sciences, Inc.) to establish ohmic contact. The steel plate was itself electrically connected to a Cu wire using CW2400 epoxy (Circuitworks/Chemtronics Inc.) to establish electrical connection and J-B Weld epoxy (J-B Weld Co.) to establish a robust mechanical connection. In Fig. 2, the reference electrode was sealed in a PTFE tube using Epofix epoxy (Struers Inc.), except where it was exposed at the ends.

The Cu/CuF reference electrode was prepared by anodization in UDHF prior to being added to the fixture, Fig. 2. After cleansing in sulfuric acid, the bare wire was biased at 1 V opposite to a Pt mesh for 5 min using a standard dc power supply. For proper bias, the Cu wire was connected to the positive terminal of the power supply and the Pt connected to the negative terminal, rendering a matte/dull reddish surface finish.

Not shown in Fig. 2, a tungsten lamp was situated above the chamber using a fixture to standardize its position with respect to the HDPE chamber. The intensity of illumination at the working electrode was measured to be roughly 250 (lux). After the lamp was positioned, the sample was allowed to equilibrate for 5 min prior to characterization. Following electrochemical characterization, the anodized dice were outgassed for 15 min at low vacuum to remove any residual electrolyte.

Results and Discussion

Morphology of the corroded surface layer.— The morphology of SOI and polySi specimens was examined in order to identify the current conditions present during corrosion, according to the amount of Au utilized. First, the surface morphology is shown to vary according to the relative surface area ratio (SAR) of Au to Si in Fig. 3. Reference specimens, i.e., etched in HF but with SAR = 0, are included in Fig. 3, which demonstrates the porous surface morphology, quantified in Table I, for SOI and Poly-1 structures etched in UDHF:Triton for 12 and 40 min, respectively. In Fig. 3, the pore shape is either circular or square with rounded corners. In Table I, the SAR (Au:Si), pore diameter, interpore spacing, thickness of the corroded surface layer, porosity, and corresponding current density (Eq. 1) are given for the specimens. The d, L, and P values in Table I are from field emission scanning electron microscope (FESEM) measurements, with t being obtained after the delineation etch in the FIB. Certain specimens (Poly-1, SAR of 10.31) proved difficult to interpret. For this and other specimens etched for longer time duration,[1] P is estimated to exceed 70%. Additionally, while a few pores were observed on the SOI reference specimen (SAR = 0), P is minor ($<5\%$); therefore the reference specimens are not examined in Table I. From Table I, an increase in thickness and porosity occurs as the SAR is increased for both SOI and Poly-1. Conversely, if the statistical variance of the measurements is considered, then the interpore spacing does not vary with SAR, instead L averages to be 12.7 ± 1.3 nm for all specimens. In Table I, t shows the strongest correlation ($\sim 5\times$ change with SAR), then P ($\sim 2\times$ change with SAR), and finally d ($\sim 1/2\times$ change with SAR). For the SOI specimens, the SAR in Fig. 3 and Table I applies to the condition where only the top surface is etched[1] and not the nominal condition (etching of all exposed surfaces). In addition to the data summarized in Table I, a correlation was observed between surface porosity and visual discoloration ranging from reddish-brown to dark gray for polySi, as well as bright purple, blue, green, yellow, and orange seen for SOI (see Ref. 30). Also, rounded particulate material was observed for several of the Poly-1 specimens (Fig. 3); their origin and composition are explored later. Additional images of micromachined Si etched in the different solutions or at lesser magnification may be found in Ref. 1 and 30.

Because porosity (pore diameter) is increased as the amount of metal present is increased, the morphology data demonstrates the significance of the SAR as a "processing parameter." This may be explained if the corrosion is current limited (e.g., by the reduction reaction occurring at the cathode). Separately, it should be cautioned that the damage seen in Fig. 3 might be identified as being under-representative. To explain, the corroded surface layer was previously found to primarily consist of Si_xO_y,[1,5-7] whereas the material is affected according to a PS formation process.[1,6,7] That is, the Si pores formed in HF will shrink upon the $2.17\times$ volumetric expansion occurring during their subsequent oxidation in the ambient environment,[18] reducing the porosity and increasing the current density. For this reason, where P is not directly measured, the value of 50% will be henceforth used to estimate corrosion current density or the thickness of affected material, Eq. 1 and 2.

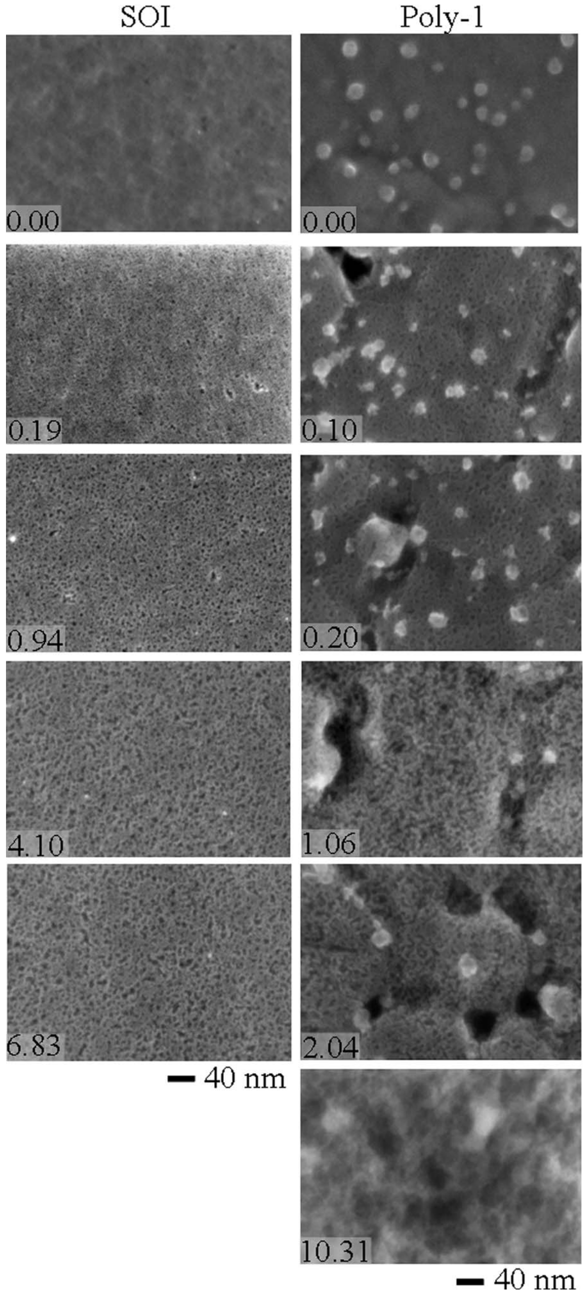

Figure 3. Surface morphology of SOI and Poly-1 as the surface area ratio (SAR) is increased. The SAR (Au:Si) is indicated for each specimen. Specimens were etched in UDHF:Triton for 12 and 40 min, respectively. For the Poly-1 specimens, particulate contamination is present in some cases (rounded or spherical features).

In comparison to the parametric test structures examined in Fig. 3, FESEM images examining the surface morphology of polySi tensile specimens[1] after being etched for 40 min are shown in Fig. 4. For the three etchants utilized, all specimens with metal present demonstrated surface pores, whereas those specimens with no metal present did not demonstrate surface porosity, except for those etched in UDHF:H_2O, which exhibited surface pores both with and without metal present. In cross-sectional scanning tunneling electron microscopy examination[1] at a particular etch time, the thickness of the corroded surface layer for specimens with metal present ranged from greatest for UDHF, intermediate for UDHF:H_2O, and least for UDHF:Triton, although the final values were within the same order of magnitude. The pore size and spacing in Fig. 4 is similar to that in Fig. 3, except that the porosity for the two specimens with metal

Table I. Summary of characteristics obtained from surface- and cross-sectional morphology observation of Poly-1 and SOI specimens, as SAR (Au:Si) is increased. Specimens were etched in UDHF:Triton for 12 and 40 min, respectively.

Technology	Layer	SAR	*d*, pore diameter (nm)	*L*, pore-to-pore spacing (nm)	*t*, thickness surface layer (nm)	*P*, porosity (%)	*j*, current density (mA/cm^2)
SOIMUMPs	SOI, 10 μm	0.19	5.7 ± 1.1	10.7 ± 2.1	25 ± 2	20 ± 7	0.011
SOIMUMPs	SOI, 10 μm	0.94	6.6 ± 1.3	11.3 ± 1.9	72 ± 2	26 ± 6	0.042
SOIMUMPs	SOI, 10 μm	4.10	8.5 ± 1.3	12.8 ± 2.0	165 ± 10	36 ± 7	0.132
SOIMUMPs	SOI, 10 μm	6.83	9.0 ± 1.8	12.4 ± 2.3	N/A	43 ± 9	N/A
polyMUMPs	Poly-1	0.10	8.5 ± 1.9	14.1 ± 2.6	42 ± 5	28 ± 7	0.008
polyMUMPs	Poly-1	0.20	8.7 ± 2.5	13.4 ± 3.7	64 ± 10	30 ± 7	0.013
polyMUMPs	Poly-1	1.06	10.2 ± 1.6	14.4 ± 3.0	108.5 ± 7	42 ± 10	0.030
polyMUMPs	Poly-1	2.04	9.5 ± 1.9	12.8 ± 3.1	144 ± 26	47 ± 10	0.045

present (UDHF:H_2O and UDHF:Triton) approaches or exceeds 70%. Lastly, as in Fig. 3, rounded particulate material was seen for several specimens (Fig. 4).

As the surface porosity in Fig. 4 corresponds to degradation in mechanical properties,[1] it is seen as direct evidence of corrosion, which is typically absent on the reference specimens without metal present. As in Ref. 31, the pores observed on the UDHF:H_2O etched specimens with no metal present suggest an influence of –OH ions, most prevalent in that solution. In this case, while pores are present and metal is not, the microtensile characterization[1] indicates that damage obtained in UDHF:H_2O is strictly limited to the immediate surface. In contrast, the similar morphology and thickness of the corroded surface layer for those specimens with metal present suggests a shared formation mechanism. For specimens with metal present, differences in the depth of chemical attack will be further explored using the resistive probe technique and then related to the surface-wetting characteristics of the etchants utilized using the sessile drop characterization.

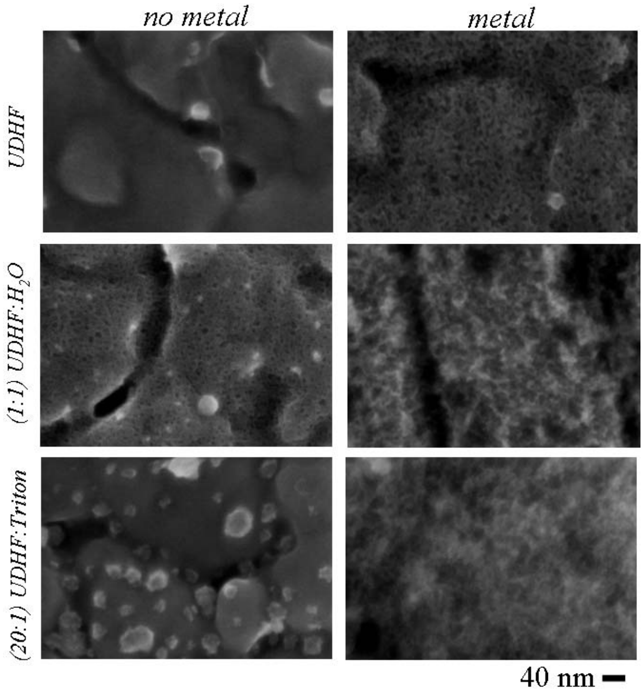

Figure 4. FESEM images showing the morphology of the top surface of Poly-1 tensile specimens[1] after being etched for 40 min. A porous network is always seen for those specimens with metal present. Particulate contamination is present in some cases (rounded or spherical features).

Current density, determined from resistance.— The resistive probe technique was used to further examine the variation of corrosion current density (determined from etch rate) according to etch time, etchant solution, and SAR. To begin, current was characterized as a function of time and etchant using Eq. 3 and 6; the results for the Poly-1 layer are shown in Fig. 5. An optical image of a resistive probe is shown in the inset of Fig. 5, with the components and composition of the structure labeled accordingly. For all etchants, the current is seen to asymptotically decrease to a "steady" value within 90 min. In Fig. 5, a double-exponential decay trendline fit is used to identify the asymptotic decay. In Fig. 5, the magnitude of the current is similar for UDHF and UDHF:H_2O, and is least for the UDHF:Triton etchant.

Additional data summarizing the resistive probe experiments are shown in Table II, identifying the maximum normalized resistance, the maximum etch rate, and the corresponding maximum corrosion current density. As in Fig. 5, the estimated rate of corrosion was always greatest initially and then decreased asymptotically with etch time. Unlike in Fig. 5, no clear distinction is found between the different etchants for the SOI layer (Table II). Although the etch time was limited to 12 min for the SOI layer by the undercutting of the SiO_2 layer that attached it to the underlying substrate, the increase in resistance for the SOI layer is comparable to that observed for the Poly-1 layer at 12 min. Although the "Poly-2" and "Poly-1 + Poly-2" layers were also measured,[30] Table II solely distinguishes between the Poly-0 and Poly-1 layers present in the polyMUMPs technology. Uniquely, the resistance became "infinite" for

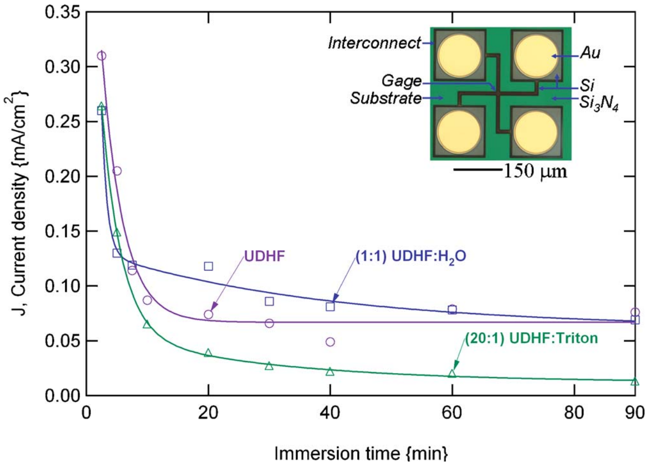

Figure 5. (Color online) Current density (for $P = 50\%$) determined using Poly-1 resistive probes for the three different etchant solutions. An optical micrograph of the test structure is shown in the inset.

Table II. Summary of resistive probe measurements for the SOI, Poly-0, and Poly-1 layers.

Technology	Layer	Etchant chemistry	$R_{\max}$, normalized resistance	$r_{\max}$, etch rate (nm/min)	$j_{\max}$, current density (mA/cm^2)
SOIMUMPs	SOI, 10 μm	UDHF	1.02	41.2	0.550
SOIMUMPs	SOI, 10 μm	UDHF:H_2O	1.05	29.0	0.387
SOIMUMPs	SOI, 10 μm	UDHF:Triton	1.02	35.9	0.479
polyMUMPs	Poly-0	UDHF	∞	∞	N/A
polyMUMPs	Poly-0	UDHF:H_2O	∞	∞	N/A
polyMUMPs	Poly-0	UDHF:Triton	1.11	3.1	0.041
polyMUMPs	Poly-1	UDHF	2.29	23.2	0.309
polyMUMPs	Poly-1	UDHF:H_2O	2.06	19.5	0.260
polyMUMPs	Poly-1	UDHF:Triton	1.12	19.8	0.264

the Poly-0 layer between 40 and 60 min, when etched in UDHF or UDHF:H_2O. The results shown in Fig. 5 and Table II are consistent with those previously obtained using simpler electrical trace structures.[12]

The behavior observed in Fig. 5 bears striking similarity to the degradation in mechanical performance measured using microtensile specimens.[1] To begin, the current profile in Fig. 5 bears the same shape over time as the profiles for mechanical strength and apparent modulus. More specifically, for UDHF or UDHF:H_2O, the average current density (etch rate) determined from resistive probe measurements is 2/3 the maximum current obtained from cross-sectional observation of the microtensile specimens. For the UDHF:Triton etchant, however, the current determined from resistive probe measurements corresponds with the current determined from the minimum thickness of the corroded surface layer. As in the resistive probe measurements, current was found to decrease with time for the microtensile specimens. For example, the maximum current density of 0.294 and 0.108 mA/cm^2 were obtained for the UDHF etched Poly-1 microtensile specimens at 20 and 90 min, respectively. The corresponding resistive probe and microtensile results are as expected, since the same SAR of 0.85 was utilized for resistive probe structures (Fig. 5), as that of the Poly-1 microtensile specimens. The correspondence between the microtensile and resistive probe structures indicates that resistive probe characterization is a reasonably accurate diagnostic/predictive technique, as long as the SAR is matched to that of a simulated device. To that end, a resistive probe could be used for the purpose of monitoring corrosion in situ, if connectivity could be established to Si in a HF solution (e.g., back side vias) and the influence of connectivity could be compensated.

As in the microtensile characterization,[1] the etchant specific damage seen in the resistive probe specimens is attributed to the physio-chemical nature of the corrosion process (Fig. 1), i.e., the surface wetting characteristics of the etchants utilized. Cross-sectional examination in Ref. 1 correlated etchants having weak surface wetting characteristics to damage dominated by surface or microstructural vulnerabilities, whereas as etchants with strong surface affinity resulted in homogeneous damage about the surface. Regarding microstructural defects, polySi was found to contain crevices, cavities, twins, and grain boundaries, whereas SOI exhibited processing-induced surface defects only.[1] Therefore, the 4× greater current for UDHF and UDHF:H_2O in Fig. 5 is attributed to microstructure specific attack, such as observed grain boundary attack,[1] whereas the lesser current for UDHF:Triton is attributed to generalized attack about the surface of Si. Thus, the assumed homogeneous damage profile for Eq. 3 is only directly applicable for UDHF:Triton and is subject to limitation (an acceleration factor) for UDHF and UDHF:H_2O.

Unlike for polySi, the SOI resistive probes are subject to a limited population of vulnerable microstructural features. Foremost, the SOI layer specifically lacks microstructural defects, precluding a microstructure specific acceleration factor. The lack of distinction between etchants for the SOI resistive probes (Table II) is further subject to the limited etch time allowed by the underlying SiO_2 layer as well as the geometry of the specimens. From the resistance measurements, the percentage of area consumed was significantly greater (up to 40–60%) for the polySi specimens, as opposed to the 2–3% maximum area consumption for the SOI specimens. Therefore, a more substantial etch time, allowing more Si to be consumed, would be expected to obviate the identification of etchant specific differences, if any could be facilitated by morphology (sidewall surface roughness).

From the data, current densities of 0.23–0.55 mA/cm^2 were determined for the SOI resistance probes etched in UDHF, whereas the value of 0.101 mA/cm^2 was obtained from a microtensile specimen etched in the same solution.[1] Disparity between the resistive probe and microtensile specimens may be explained by the stray etching observed at the top corner of the sidewall surfaces.[1] That is, in cross-sectional examination, corrosion affects the top surface of SOI but also extends onto the sidewall surfaces by as much as 1 μm. Therefore, as the top surface is solely considered in Eq. 4, the actual current for the resistive probes is likely to be lesser than that shown in Table II.

A series of Poly-1 resistive probes was also used to investigate the significance of the SAR, shown in Fig. 6. As shown in the inset of Fig. 6, the polySi structure remained the same, but the amount of metal present was varied parametrically. The SAR values (Au:Si) of 0.05, 0.21, 0.85, and 3.39 were specifically examined. Because the

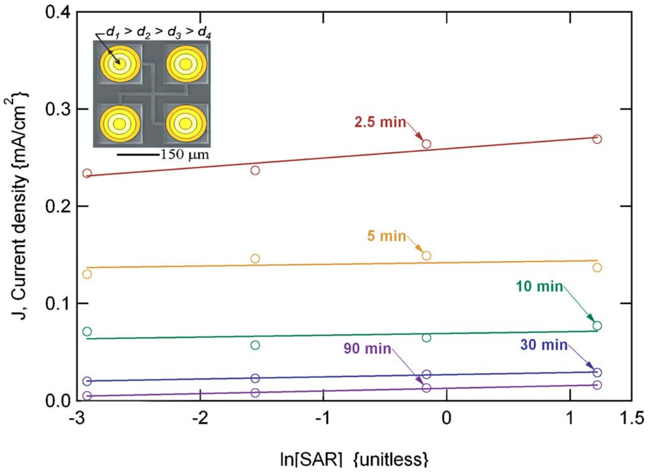

Figure 6. (Color online) Current density (for $P = 50\%$) as a function of SAR (Au:Si), from Poly-1 resistive probes etched in UDHF:Triton. The proportion of surface area for Au relative to Si was varied according to the amount of Au present (inset). Data are shown for a series of probes etched for 2.5, 5, 10, 30, and 90 min.

current increased exponentially with SAR at the different etch times examined, a linear trendline fit for logarithmic variation is shown in Fig. 6. For a particular SAR, the current decreases asymptotically with time as in Fig. 5, whereupon the initial and final data points at 2.5 and 90 min differ by a factor of 4–5. Figure 6 applies to the UDHF:Triton etch chemistry, but similar behavior was observed for the other etchants. As in Fig. 5, current within this parametric study was determined to vary according to etchant solution, with the final measurements for UDHF and UDHF:H_2O being 4 times that of UDHF:Triton.

As in the damage morphology examination, Fig. 3 and Table I, a correlation is identified in Fig. 6 between SAR and corrosion. The resistive probe data, which spans a greater range of SAR values than Table I, allows for a more definitive relationship to be established. In Fig. 6, the current varies logarithmically with SAR (as in an exponential or Arrhenius relationship), consistent with the thickness variation in Table I. The variation in Fig. 6 explicitly identifies that the corrosion of Si is limited by corrosion current [i.e., the size of the cathode (Au)].

Figure 7, which generalizes the data for polySi etched in UDHF or UDHF:H_2O, will be used to summarize and further interpret the resistive probe measurements. In regime I of Fig. 7, the average etch rate decreases in an asymptotic manner. Because this regime occurs to a similar extent in all polySi as well as SOI specimens, it is identified as a universal initiation regime. Similar to Fig. 7, a high-impact initiation period (regime I) is also identified in the microtensile tests,[1] where strength is notably decreased within 5 min. The similar magnitude of change observed in Fig. 5 is therefore suggested to be associated with the formation of a porous surface layer. This process would quickly concentrate charge at the active etch front for all specimens and etchants until the influence of surface wetting combined with microstructural defects becomes influential over time.

As it has been suggested the distribution of dopant is not uniform for extrinsic Si [dopant may accumulate up to 20× the bulk concentration at the free surface(s)],[32-36] the high current seen in regime I may also be affected by the dopant concentration. Attributed to lattice mismatch, a 5 nm thick dopant-rich region may form at the interface between Si and a deposited oxide,[32] thermally grown oxide,[33,34] or native oxide.[35,36] For phosphorus, where the dopant must carry an associated vacancy neighbor to remain electrically neutral, the surface region would be rendered particularly reactive because of the resulting lesser atomic coordination number in the surrounding silicon. In polySi, dopant may also accumulate at grain boundaries,[13,35] which would affect corrosion after the initiation regime. Surface-specific dopant segregation effects would, however, affect all etchants equally in regime I. Here, for example, dopant concentration at the surface may influence the time required for stabilized pore morphology to form.

Regime II in Fig. 7, which shows minor attenuation in etch rate over time, is attributed to stabilized steady-state corrosion. To explain, once a porous corroded surface layer has formed, the magnitude of the damage should relate to the physio-chemical activity at the active etch front (Fig. 1). Here, the physical effects of steady-state corrosion are inferred from the cross-sectional observation of the microtensile specimens.[1] In that study, UDHF renders deep, sporadic crack propagation along grain boundaries. Alternately in UDHF:Triton, steady-state corrosion results in uniform, generalized consumption of both polySi and PS. This is because the superior wetting characteristics of UDHF:Triton result in damage that is distributed throughout the active etch front, rather than bearing preference specific to defects and surface morphology. In Fig. 5 and Table II, the comparable extent of damage between UDHF and UDHF:H_2O is attributed to their similar wetting characteristics. The data for UDHF and UDHF:H_2O in Fig. 5 is, however, much more comparable than for the microtensile specimens. Therefore, the resistive probe results suggest that additional latent damage, i.e., grain boundary attack or degradation of the interior, is present for UDHF:H_2O than was readily apparent in the damaged microtensile specimens. In contrast, the more stable and significantly lesser magnitude of damage in Fig. 5 for UDHF:Triton owes to its improved surface wetting, and implies that the interior of the polySi remains intact, which is corroborated in the microtensile specimens.

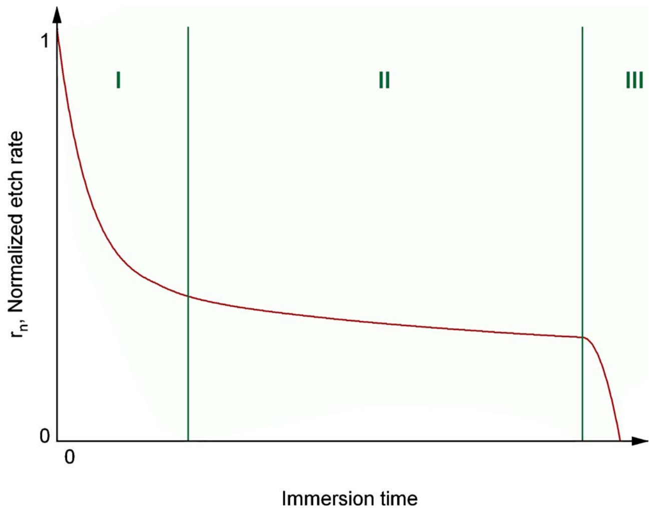

Figure 7. (Color online) Schematic representing variation in average etch rate with time for polySi etched in UDHF or UDHF:H_2O. Three separate behavior regimes are identified in the figure.

The results in regime II are contrary to the literature, where the thickness of the corroded surface layer was observed to increase linearly for a fixed current density.[9] Assuming current generation at the cathode is not affected over time, the attenuating current in Fig. 5 and Table II may occur as the result of (*i*) decreased electrical connectivity facilitated by grain boundary attack, (*ii*) the completed consumption of the most reactive regions of Si, or (*iii*) limited transport of reactants/products through the thickening corroded surface layer. Regardless of the exact cause of time-attenuated current, the different rates of damage seen in Fig. 5 primarily result from the wetting characteristics unique to each etchant.

Finally, for Poly-0 etched in UDHF or UDHF:H_2O, measured catastrophic failure is identified in Fig. 7 as regime III. Behavior here is attributed to compromised electrical connectivity, when Si is either severed at grain boundaries or completely corroded. Only a single electrical break need be established across the gauge section to terminate the process of galvanic corrosion (i.e., 100% volumetric degradation is not required). Catastrophic failure was additionally observed for Poly-0 electrical trace structures (two point probe technique) etched in UDHF or UDHF:H_2O.[12] Although not observed for the other polySi layers,[30] similar catastrophic failure is expected after a sufficient etch time. As in regime II, observed catastrophic failure also suggests extensive latent damage for the UDHF:H_2O etchant that is not directly observed for microtensile specimens. In comparison, catastrophic failure was only observed for microtensile specimens etched in UDHF, which fractured autonomously in solution after 90 min.[1]

Contact angle of HF-based solutions.— Contact angle measurements were performed to validate the assumed surface wetting characteristics for the etchants utilized. Table III shows the results of the sessile drop characterization, which compares the surface wetting characteristics of the three etchants to that of deionized (DI) water. Table III includes measured contact angle and the specific work of adhesion, determined to within ±2.6° and ±0.04 [2 standard deviations (SD)], respectively. For the purpose of discussion, contact angles $\leqslant 30°$ will be considered hydrophilic, whereas contact angles $\geqslant 60°$ are considered hydrophobic. In Table III, the work of adhesion has been normalized to that of DI on (111) SCS (the lowest energy orientation[37]), where γ_{lv} is taken as the same for all solutions (i.e., the specific work of adhesion is an approximation for the pur-

Table III. Contact angle and specific work of adhesion [normalized to DI water on (111) Si] for SCS, polySi, and PS, measured by the sessile drop technique. A generalized schematic of a droplet viewed in cross section is shown in the inset.

Substrate	Etchant	θ, contact angle (deg)	$W_{a,sp}$, specific work of adhesion
(100) SCS	UDHF	63	1.06
(100) SCS	UDHF:H_2O	73	0.94
(100) SCS	UDHF: Triton	12	1.44
(100) SCS	DI	74	0.93
(111) SCS	UDHF	67	1.01
(111) SCS	UDHF:H_2O	71	0.97
(111) SCS	UDHF: Triton	10	1.44
(111) SCS	DI	68	1.00
polySi	UDHF	46	1.23
polySi	UDHF:H_2O	68	0.99
polySi	UDHF: Triton	10	1.44
polySi	DI	72	0.96
(100) PS	UDHF	65	1.03
(100) PS	UDHF:H_2O	73	0.94
(100) PS	UDHF: Triton	11	1.44
(100) PS	DI	81	0.84

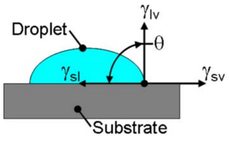

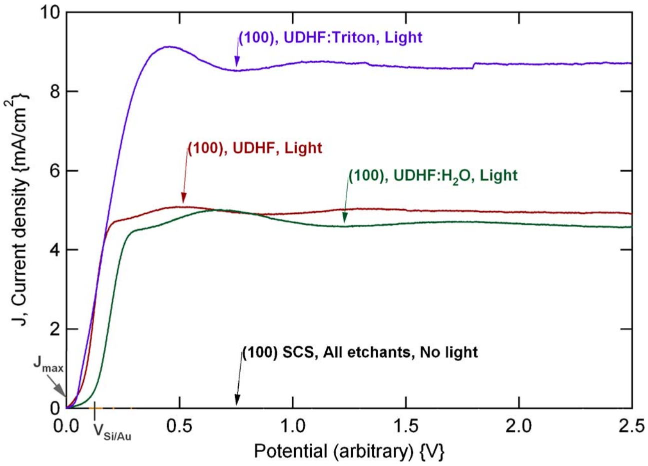

Figure 8. (Color online) Comparison of polarization curves for (001) SCS anodized in three separate solutions, with and without light present. The bounds of the mixed pair potential, $V_{Si/Au}$ and maximum current density, J_{max}, are indicated in the figure based on the literature and previous (morphology, resistive probe) characterizations.

pose of generalized comparison). The contact angle for polySi (both Poly-0 and Poly-1 are averaged) was found to be less than that of the other specimens, particularly for UDHF (Table III). Within a particular Si group, the contact angle was typically seen to range from least to greatest for UDHF:Triton, UDHF, UDHF:H_2O, and then DI, respectively. Physically, the decreased contact angle for UDHF:Triton identifies a greater work to wet the droplet to the substrate, whereas the large contact angle for UDHF:H_2O indicates a lesser surface wetting relative to UDHF (Table III). During characterization, UDHF:Triton uniquely demonstrated a slow change in location about Si as time elapsed. For reference, the contact angle of DI on a Si native oxide was found to be 44°.

Surface roughness is thought to explain the reduced contact angle for polySi relative to that of SCS. Increased surface roughness is known to decrease contact angle, as long as the contact angle is initially $<90°$.[38] Specifically, the roughness of the polySi samples is 8.5 ± 11.4 nm, whereas that of the SCS is 0.1 ± 0.1 nm ($R_{avg} \pm R_{rms}$).[23] In comparison, the contact angle is seen to be similar for (100) SCS and (111) SCS, despite their different surface free energies.[37] Therefore, the difference in contact angle between the various Si specimens is attributed to their surface roughness and not crystallographic anisotropy.

Regarding the etchant specific variation in surface wetting, an increase in HF concentration was found to correspond to increased surface affinity.[39] Specifically, Roth et al. found that the surface tension, $\gamma = \gamma_{lv}$, continuously decreased as HF concentration was increased, consistent with the measurements in Table III for DI, UDHF:H_2O, and UDHF. Alternately, as a surfactant is added to HF, surface tension will be decreased until the critical micelle concentration (CMC) of the surfactant is achieved,[39] with the overall effect on surface wetting being quite significant. Therefore as expected, the surface wetting for UDHF:Triton was greatly improved for all Si types. It should be noted that the UDHF:Triton solution in Table III is significantly above the CMC concentration ensuring that surface wetting is maximized to both Si and PS [at the expense of nanoscale particulate contamination (i.e., micelle formation)].

The contact angle data (Table III) and Pourbaix (potential/pH) diagram in Ref. 7 and 11 suggest that UDHF:H_2O should be less influential than UDHF, based on its poor surface wetting (limiting the flux of reactant species) and its greater Gibb's free energy potential (indicating that corrosion is less thermodynamically favored). The performance of microtensile specimens etched in UDHF:H_2O, however, was intermediate to the other two etchants.[1] As confirmed in cross-sectional observation,[1] the poor surface wetting characteristics for UDHF:H_2O (Table III) primarily result in microstructure specific attack, such as grain boundary attack. Microstructure specific attack is also implied in the resistive probe measurements, Fig. 5 and Table II, where UDHF:H_2O was similar to UDHF (the etchant most prone to grain boundary attack). However, for UDHF and UDHF:H_2O, the difference in etch rate is further influenced by the separate issues of viscosity and hydroxide ion concentration. Although the increased viscosity (0.87 for UDHF:H_2O vs 0.80 mN s m^{-2} for UDHF[40,41]) might be expected to slightly retard or localize corrosion for UDHF:H_2O, FESEM images of the surface morphology (Fig. 4), suggest instead that the effects of the hydroxide ions dominates, enhancing the rate of Si consumption. To explain, a porous surface is generated on Si etched in UDHF:H_2O, even when no metal is present, indicating enhanced corrosiveness for UDHF:H_2O. The notion of –OH related catalysis or the involvement of hydroxide in Si corrosion has been identified by others.[31,42] For the case of galvanic corrosion, the increased chemical activity for UDHF:H_2O explains the wider features observed in cross-sectional examination.[1] Additionally, the dimensions of UDHF:H_2O etched samples with metal present were found to be slightly reduced in size,[1] suggesting that UDHF:H_2O acts upon PS as well as Si. If PS is consumed in addition to Si, then the active etch front advances less rapidly, reducing the overall damage rate. In summary, the poor surface wetting for UDHF:H_2O is explained to initially result in microstructure specific attack, with the rate of corrosion being slightly retarded by mass transport (the greater viscosity of the etchant). For prolonged exposure, the greater hydroxide ion concentration for UDHF:H_2O, yields more broadly distributed damage, moderating the impact of corrosion.

Electrochemical characterization: OCP and polarization curves.— A series of electrochemical characterizations, including OCP measurements, cyclic voltammetry (polarization profiles), and chronopotentiometry data, was conducted to quantify the kinetic response for Si according to the three etchants utilized. Except for OCP, a complete set of data was obtained for SOI, Poly-0, Poly-1, and (100) SCS; the essential results are shown in Fig. 8-12. To aid their discussion, the morphology characterization, resistive probe results, and contact angle measurements will be utilized in order to interpret the various electrochemical examinations and their application to the previous microtensile mechanical study.[1]

To begin, OCP measurements for the (100) SCS dice, Au wire, or the Pt counter electrode mesh were averaged for the UDHF,

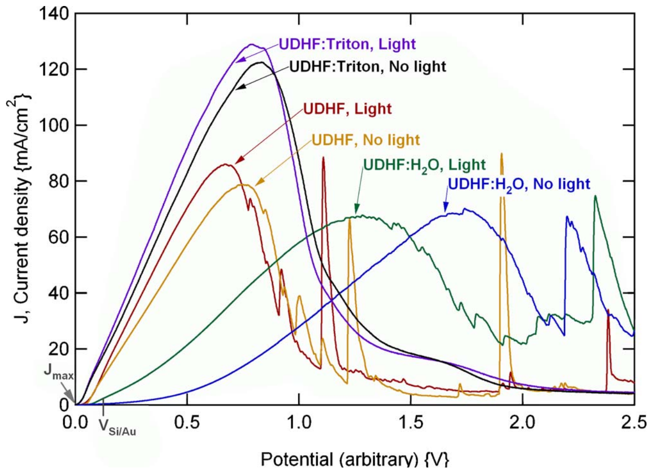

Figure 9. (Color online) Comparison of polarization curves for SOI anodized in three separate solutions, both with and without light present. The bounds of the mixed pair potential, $V_{Si/Au}$ and maximum current density, J_{max}, are also indicated in the figure.

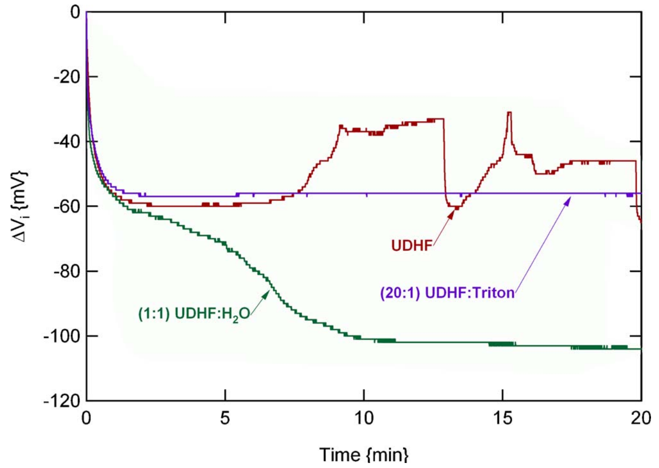

Figure 11. (Color online) Chronopotentiometry results ($j = 0.25$ mA/cm^2) for SOI anodized in three separate solutions, with light present.

UDHF:H$_2$O, and UDHF:Triton etchants (i.e., three separate measurements for each material). Relative to the Cu/CuF reference electrode, the OCP values of −0.47 ± 0.06, 0.43 ± 0.11, and, 0.70 ± 0.06 V (1SD) were measured for Si, Au, and Pt, respectively. OCP did not vary significantly between Si specimens, but was measured to be −0.48 ± 0.06, −0.42 ± 0.02, and −0.52 ± 0.04 V (1SD) for Si when immersed in the UDHF, UDHF:H$_2$O, and UDHF:Triton etchants, respectively. In contrast, OCP was previously seen to vary slightly with the etchant utilized.[2,3] The potential difference between Au and Si here is similar to that described by others.[5-7] Compared to the literature, the experiments therefore suggest that the OCP of the Cu/CuF reference electrode is −0.24 V_{SCE}, whereas the value of −0.271 V remained stable in UDHF for 15 min when measured against a standard Ag/AgCl reference electrode (saturated KCl) using a salt bridge (i.e., −0.227 V_{SCE}). This is similar to the value of 0.276 V, measured by others for a Cu/CuF electrode in anhydrous HF using a hydrogen reference electrode, where the measured potential was found to be stable and was attributed to the formation of a CuF$_2$ surface layer.[43,44]

Polarization curves were obtained at the rate of 20 mV/s and are shown for SCS, SOI, and Poly-1 in Fig. 8-10, respectively. These figures compare the electrochemical response with and without light present for the different Si specimens, when anodized in the three etchants. The voltage potential in the polarization plots is not absolute; rather it is shown relative to the asymptotic increase in current density just above the background limit, so as to accentuate the difference between the data profiles. In all figures, the current density indicated applies to the nominal (entire) test area region. The voltage increase corresponding to the mixed pair potential in the literature ($V_{Si/Au}$ of 150 mV) as well as the maximum current density observed in the morphology of microtensile specimens (J_{max} of 0.294 mA/cm^2) is indicated in the figures. The response for Poly-0 and Poly-1 differed primarily in magnitude, therefore only Poly-1 is shown (Fig. 10). Unlike in the figures, no Si corrosion was observed under cathodic polarization conditions (i.e., applied potential below the OCP of Si). Lastly, the visual appearance of the specimens after polarization featured fully anodized test areas.

Regarding the use of light, a specific response is observed only for (100) SCS (Fig. 8). For (100) SCS, the magnitude of the current present scaled according to the proximity of light source, and no measurable current was detected in the absence of illumination. Additionally, (100) SCS demonstrated a Zener (reverse) breakdown voltage of 14.1 ± 0.9 V in the dark. In contrast, the response for SOI and Poly-1 did not vary significantly with illumination. Instead, the polarization profiles were only slightly decreased in magnitude and somewhat more sluggish without illumination (Fig. 9 and 10).

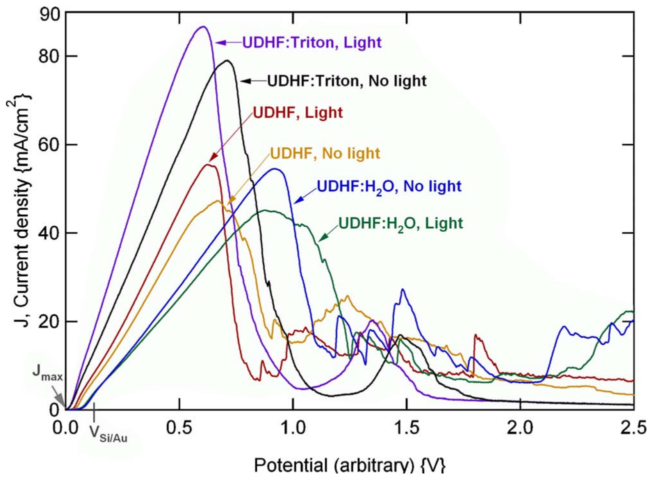

Figure 10. (Color online) Comparison of polarization curves for Poly-1 anodized in three separate solutions, both with and without light present. The bounds of the mixed pair potential, $V_{Si/Au}$ and maximum current density, J_{max}, are also indicated in the figure.

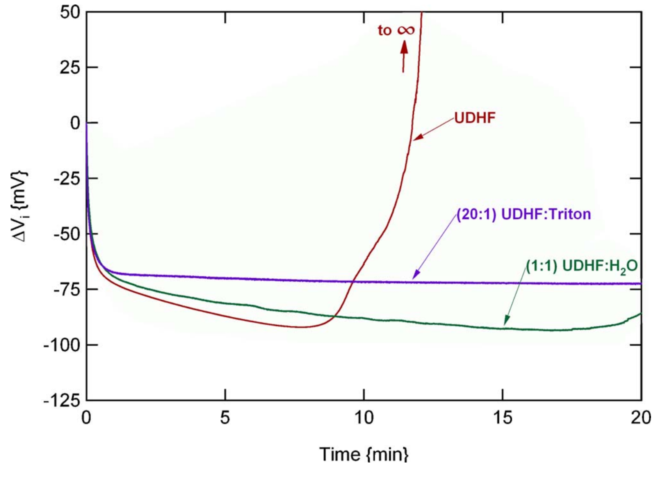

Figure 12. (Color online) Chronopotentiometry results ($j = 0.25$ mA/cm^2) for Poly-0 anodized in three separate solutions, with light present.

Table IV. Key results from polarization characterization. The current density and surface layer thickness at the onset of electropolishing (with illumination present) are indicated. An asterisk is used to indicate that the (100) SCS data applies only when illumination is present.

Technology	Layer	Etchant chemistry	Current without illumination	$j_{\max}$ (mA/cm^2)	$t_{\mathrm{CSL,EP}}$ (μm)
SCS	(001)	UDHF	N	5.1*	0.1*
SCS	(001)	UDHF:H_2O	N	5.0*	0.1*
SCS	(001)	UDHF:Triton	N	9.1*	0.2*
SOIMUMPs	SOI, 10 μm	UDHF	Y	86.1	1.9
SOIMUMPs	SOI, 10 μm	UDHF:H_2O	Y	67.8	2.6
SOIMUMPs	SOI, 10 μm	UDHF:Triton	Y	128.9	3.5
polyMUMPs	Poly-0	UDHF	Y	32.3	0.2
polyMUMPs	Poly-0	UDHF:H_2O	Y	34.2	0.3
polyMUMPs	Poly-0	UDHF:Triton	Y	46.7	0.4
polyMUMPs	Poly-1	UDHF	Y	55.5	1.0
polyMUMPs	Poly-1	UDHF:H_2O	Y	45.1	1.2
polyMUMPs	Poly-1	UDHF:Triton	Y	86.7	1.8

Within the polarization profiles, a consistent set of characteristics can be used to distinguish between the etchants and Si examined. Regarding the magnitude of corrosion current, the greatest current was consistently observed for UDHF:Triton, approaching double that of the other etchants. Between UDHF and UDHF:H_2O, a more rapid response and greater maximum current was observed for UDHF. In particular, the response for UDHF:H_2O is notably slower for SOI than the other Si types (Fig. 9). Regarding the different Si specimens, the peak current ranged from greatest to least for Poly-1, SOI, then Poly-0, respectively. The peak in the profiles in Fig. 9, and Fig. 10 at $\sim$0.5 V is consistent with the onset of EP in the literature.[2,3,5-11] For UDHF and UDHF:H_2O, the behavior beyond the peak current features an erratic profile (current spikes), which varied considerably between repeated characterizations. In contrast, the behavior beyond the peak current for UDHF:Triton was both stable and repeatable. Key results are further summarized in Table IV, which includes the effect of illumination. Also, the maximum current density ($j_{\max}$) and thickness of the corroded surface layer ($t_{\mathrm{CSL,EP}}$, from Eq. 2 for the integrated polarization data) at the peak current are provided. In Table IV, an asterisk is used to indicate that the (100) SCS data applies only when illumination is present.

In contrast to the other specimens, the (100) SCS samples do not demonstrate electropolishing behavior in Fig. 8, which is related to their specific response to light. To explain, for lightly doped n-type Si (n^-), illumination is required to facilitate the supply of holes[9,18] (Fig. 1). Conversely, for very highly doped n-type Si (n^+), illumination is not required,[9] as its Fermi level lies within the conduction band, rendering metal-like electrical characteristics for the "degenerate" Si.[11] Conversely, photoelectrochemistry is not typical for p-type Si, which is expected to corrode regardless of illumination, because its semiconducting (p/n) characteristics are opposite that of n-type Si.[9] For (100) SCS, the illumination provided is simply not sufficient to support EP. The minimal influence of illumination for the micromachined Si (SOI, Poly-0, and Poly-1 in Table IV) is distinctly different from the behavior in Ref. 2, 3, and 6, where no corrosion current was observed in the dark. The specimens examined in the literature were either reported[2,3] or are presumed[6,7] to be less doped than those reported in Table IV. From Table IV, the transition to the degenerate regime for phosphorus-doped Si occurs for resistivity between 0.015 and 0.005 Ω cm, consistent with the literature.[45,46]

The surface-wetting characteristics of the different etchants explain many of the measured differences observed in the polarization profiles. To begin, the greater current observed for UDHF:Triton is attributed to its improved wetting characteristics (Table III), which allows a greater area of the otherwise hydrophobic anode surface[47] to be continuously anodized. Furthermore, as the data profiles for UDHF:Triton are always smooth during EP, the erratic behavior observed for the other etchants is attributed to the loss of hydrogen bubbles from the anode surface, a known benefit of the Triton surfactant.[8,9,11] Enhanced corrosion current, attributed to improved wetting characteristics, was also observed in the microsystems literature[2,3] when Triton or ethanol was added to HF. Improved surface wetting to PS, Table III, boosts current because the PS contributes additional anode surface area. As can be seen in the damage morphology (Fig. 4), current density (Fig. 5), and mechanical performance (Ref. 1 and 30), the overall impact for UDHF:Triton is moderated despite its greater current density, because both Si and PS are consumed homogeneously over a large area.

The polarization profiles for UDHF and UDHF:H_2O bear characteristics consistent with the inferior surface wetting for the etchants. To begin, the lesser current for these etchants is explained as the size of active anode is limited by bubbles and poor wetting. Therefore, in practice, etching is more specific to the surface or microstructural defects of Si.[1,30] In Table III, UDHF:H_2O bears even worse surface wetting than UDHF, further promoting microstructure specific damage and reducing the active anode area. The enhanced activity associated with the increased hydroxide concentration of UDHF:H_2O, however, counteracts poor surface wetting over time. UDHF:H_2O also bears the greatest viscosity of the etchants utilized, reducing mass transport, lending to a more sluggish response. As observed in the literature for HF diluted with water,[8] reduced ion transport also results in a greater propensity to electropolish, consistent with the reduced maximum current for UDHF:H_2O in Table IV.

Upon integration, the data profiles suggest the polySi layers are nearly fully consumed during characterization. From Eq. 2, the thickness of material consumed at the onset of electropolishing, $t_{\mathrm{CSL,EP}}$ in Table IV, approaches the known thickness of 0.5 and 2.0 μm for the Poly-0 and Poly-1, respectively. As a consequence, the true maximum current density, $j_{\max}$, may not have been attained during the experiments, particularly if an acceleration factor related to microstructure specific attack is considered for UDHF or UDHF:H_2O. To explain, a 4× acceleration factor was observed in Fig. 5 for Poly-1, which is exposed to HF at both its top and bottom surfaces, whereas the bottom surface of Poly-0 is attached to the substrate (unexposed to HF), implying a 2× acceleration factor. Visual inspection of the Poly-1 specimens identified cracked and blistered regions within the anode, validating the $t_{\mathrm{CSL,EP}}$ estimates in Table IV. In retrospect, the scan rate of 20 mV/s, chosen specifically to examine the steady state response of the Si/electrolyte interface for Poly-1 within the PS formation regime, may provide limited examination of the EP response of polySi. Of the micromachined Si specimens, the SOI layer has an inherently greater capacity (10 μm thickness) to sustain corrosion damage.

Lastly, the polarization curves can be compared against the conditions associated with galvanic corrosion. From the literature,[5-7] the potential of 150 mV, associated with a Au:Si mixed-pair, is indicated in Fig. 8-10. From the data at 150 mV, a corrosion current density as great as 20 mA/cm^2 may exist for the voltage controlled condition (Fig. 9 and 10). Alternately, the active corrosion current density may be estimated from the cross-sectional morphology in Table I, current density for resistive probes in Table II, or the cross sections of the microtensile specimens.[1] For these different characterizations, Eq. 1 suggests a maximum corrosion rate of 0.132, 0.550, or 0.294 mA/cm^2, respectively. In comparison, the average current density for these various structures typically ranges from 0.02 to 0.20 mA/cm^2. These average current density values are consistent with those observed in the literature for Si dice with Au present.[2,3,5-7] Therefore, the current density of 0.25 mA/cm^2 is shown in the polarization profiles as a conservative (worst case) estimate of the typical current limited condition. Foremost, the $V_{\text{Si/Au}}$ and J_{max} bounds in the figures solidly establish that corrosion occurs within the PS formation regime and not the mass transport limited EP regime. As J_{max} is considerably less than that allowed by the mixed pair potential, the corrosion current density estimates imply that the corrosion of micromachined Si occurs according to the current limited condition [e.g., as motivated by the size of the cathode (the SAR)].

Electrochemical characterization: Chronopotentiometry.— Chronopotentiometry characterization shown in Fig. 11 and 12 explicitly examines the current limited condition for Si with light present. Figures 11 and 12 show the measured potential difference, relative to the mixed-pair potential, in response to the externally applied current density of 0.25 mA/cm^2. Because the mixed-pair voltage varied slightly according to test conditions, voltage is shown in Fig. 11 and 12 relative to its initial potential value (i.e., voltage increase above the OCP). For the specified current, a nominally 0.38 μm thick region of Si (Eq. 2) is expected to be affected at the end of the 20 minute duration. For Fig. 12, the affected thickness increases to 0.76 μm if the 2× acceleration factor related to microstructure specific attack for UDHF or UDHF:H_2O is considered. Regarding all of the samples characterized: after 20 min, the coverage and uniformity about the test area was visually observed to be good, except for the (100) SCS specimens etched in UDHF and UDHF:H_2O.

Similar to the data shown in Fig. 12 for UDHF:H_2O, the measured potential for UDHF and UDHF:H_2O most often resembled a double exponential decay, becoming more similar to the OCP of Si over time. That is, the voltage typically quickly decreased within the first 2.5 min and then more gradually stabilized throughout the test. In contrast, a single asymptotic convergence of lesser magnitude was always observed for UDHF:Triton, which remained unchanged after 2.5 min. For the SOI layer etched in UDHF, the voltage varies chaotically after etching for ~7.5 min (Fig. 11), with the response profile varying considerably between repeated examinations. For SOI etched in UDHF:H_2O, a complicated profile (rather than the typical double asymptotic trend) is observed. In Fig. 12, a sharply increased potential was observed for Poly-0 etched in UDHF after 9 min. This increase in potential, which quickly exceeded the instrument limits, was repeatable between specimens.

As the measured voltage relates to the thermodynamic favorability, the chronopotentiometry experiments provide additional insights regarding the evolution and stability of the corrosion process. The figures suggest that the UDHF and UDHF:H_2O etchants are (*i*) inherently less stable (as evidenced by erratic behavior), (*ii*) prone to time-dependent evolution (revealed as more complicated data profiles), and (*iii*) continuously evolving (the response seldom stabilizes completely within 20 min). The erratic profile seen for SOI etched in UDHF could be explained from the time varied population of hydrogen bubbles (Fig. 1b), about the active surface. Additionally, the complicated behavior profile seen for SOI etched in UDHF:H_2O is explained from the time-dependent evolution of the liquid-solid interface across the test region, particularly because <100% coverage was visually observed after characterization. For this etchant, poor surface wetting may initially result in a limited active anode area that later becomes improved as the increased activity associated with its greater concentration of hydroxide ions is realized. In contrast, the potential observed for UDHF:Triton is both continuous and stable (attributed to its improved surface coverage), which is desirable when the corrosion of Si is to be mitigated or controlled. In addition to the surfactant, the anodization conditions utilized (low-current and -potential) should automatically reduce the magnitude of damage, possibly at the expense of instability and uniformity of coverage.

On the basis of their striking similarity, the chronopotentiometry figures will now be interpreted with the aid of the resistive probes and microtensile characterizations. As in Fig. 11 and 12, rapid asymptotic behavior is observed within 2–5 minutes for the resistive probes (Fig. 5), as was the strength rapidly decreased within the first 5 min of the microtensile characterization.[1] The similar behavior between the different characterizations suggests a common root cause. As before, this shared behavior is associated with the initiation of corrosion (i.e., the process of pore formation, universal to all Si specimens and etchant chemistries examined). The initiation period of 2.5 min is alarming, as it is shorter than the etch time used for most MEMS components. Furthermore, the chronopotentiometry, resistive, and tensile data universally imply the greatest current will occur on initiation, making the incipient etch period critically important.

After initiation, depending on the type of Si and the etchant utilized, a steady asymptotic, erratic, evolving, or stabilized behavior trend may follow. Although Fig. 12 was obtained using an applied constant current and not the time-decreased current implied in resistive probe and microtensile measurements, it does suggest that regime II in Fig. 7 is enabled by the choice of etchant (i.e., surface wetting). For polySi etched in UDHF, the effects of corrosion are dominated by the propagation of "cracks" along microstructural defects.[1] Therefore, the decrease in potential observed during chronopotentiometry is likely facilitated by charge concentration at the sharp and localized features of the propagating etch front. The activity for UDHF:H_2O is similar to UDHF as it quickly wets to high-energy defects, but it is also affected by its greater population of hydroxide ions and its greater viscosity. In particular, the hydroxide ions aid the etching of Si, broadening cracks and crevices, thereby promoting a more generalized attack over time. The chronopotentiometry (Fig. 12) and resistive probe (Fig. 5) measurements however suggest that UDHF:H_2O and UDHF are more similar than was indicated in the microtensile characterization.[1] In contrast, the activity for UDHF:Triton, which was found to correspond to generalized corrosion about the active surface,[1] is quite stable over time as facilitated by its superior surface wetting.

Lastly, further distinction may occur for more prolonged etching. Although not identified in the 20 min experiments here, steady-state corrosion may slowly decrease in an asymptotic manner, and eventually become diffusion limited (e.g., by the supply of HF, accumulation of hexafluorosilicic acid, or transport of electric charge through the anode material). In the case of Poly-0 etched in UDHF (Fig. 12), an infinite potential jump is observed, explaining regime III in Fig. 7. This is attributed to compromised electrical connectivity caused by delineation of grains along their boundaries. The amount of material predicted to be affected by the applied current is consistent with compromised electrical connectivity for Poly-0.

Morphology of anodized specimens.— To examine the effects of an applied constant current, the surface morphology of the SOI, Poly-0, and Poly-1 chronopotentiometry specimens were examined using the FESEM. Regions both within and outside of the anodized area are shown in Fig. 13 for Poly-0. In the figure, the grain structure of the Poly-0 material bears its characteristic bimodal distribution, consisting of both round and oblong grains that are highly delineated at their surface. Compared to the 2 μm thick Poly-1 layer, which is examined specifically in Ref. 1, the 0.5 μm thick

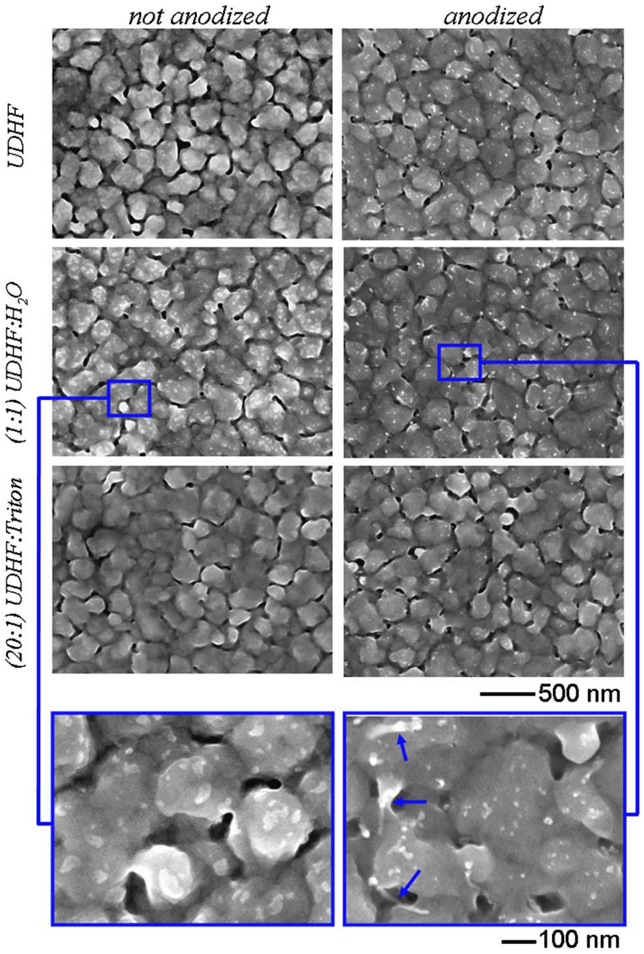

Figure 13. (Color online) FESEM images of morphology for Poly-0 after chronopotentiometry at $j = 0.25$ mA/cm^2 for 20 min in three separate solutions. Arrows in the inset indicate cylindrical particulates.

Table V. Chemical composition at the top surface of corroded Poly-0. XPS was performed on a 2 cm × 2 cm anodized die and is compared against EDX (at 10 kV) and Auger measurements of micromachined structures. The approximate spot size and maximum resolution are shown for each technique, respectively.

Elemental composition (at %)	Measurement technique XPS	 EDX	 Auger
Si	41.09	84	5.6
O	34.42	1	27.9
C	23.58	15	65.2
N	0.74	0	0
F	0.17	0	0
Surface spot size	1 mm	100 μm	100 μm
Detection Limit (at %)	0.002	0.2	0.02

Poly-0 layer also bears a greater surface roughness[12] and is presumed to be more highly doped with phosphorus, based on its lesser electrical resistivity.[23] As shown in the insets of Fig. 13, a fine surface texture (nodules as large as 50 nm) was observed for all specimens, whereas cylindrical particulates were uniquely seen on the anodized region (further indicated with arrows). Although not shown here, the surface morphology of the SOI and Poly-1 material bore a similar appearance to that seen in Fig. 3. Specifically, while both materials demonstrated a porous morphology unique to the anodized region, grains were less delineated for Poly-1, whereas no other distinct features seen at the surface of SOI. In addition to electron microscopy, the anodized region uniquely demonstrated an indigo, green, or red optical discoloration for SOI, Poly-0, and Poly-1, respectively, in an optical microscope, attributed to phonon confining/quantum emitting nanoscale crystallites within contained within an oxidized PS matrix.[1]

Foremost, the morphology seen in Fig. 3 is consistent with PS formation and not EP, where a substantial change in surface morphology would be expected as the result of the competing processes of thick oxide formation and subsequent etching. Rather, the Si is initially damaged at its surface via pore formation, whereupon the active etch front propagates into the material. Furthermore, no overt damage was seen during the microscopy examination of the UDHF etched specimen, consistent with the catastrophic failure in Fig. 12 being caused by grain boundary attack.

Because of the cylindrical particulates seen in Fig. 13, X-ray photoelectron spectroscopy (XPS) examination was used to identify any unique chemical content on the 2 cm × 2 cm die anodized in UDHF. Likewise, microsystems Si galvanically corroded in UDHF was examined using energy dispersive X-ray (EDX) and Auger electron microscopy. The chemical species identified, approximate spot size utilized, and measurement resolution are given in Table V. In all cases, the primary constituent materials of Si, O, and C were identified. It should be noted that the different conditions used during the separate examinations will yield different excitation volumes, which may be more favored toward either the surface (XPS, Auger) or interior (EDX).

Although the separate composition examinations in Table V were not as systematically conducted as the other characterizations, no exotic chemical species were identified. For example, carbon may naturally accumulate at the surface over time in the ambient environment. Additionally, fluorine may reside as Si–F surface termination after HF etching, as suggested when fluorine was also detected for microtensile specimens using cross-sectional EDX.[1] Therefore, the ubiquitous nodular surface texture (Fig. 3, 4, and 13) as well as the particulates unique to the anodized region (Fig. 13) are thought to be composed of Si_xO_y. For example, nodules at the surface could be rendered free by HF and even be partially transported as the result of their own buoyancy and/or heat exchange within the solution (the etching of SiO_2 by HF is highly exothermic). Following HF immersion, subsequent oxidation is expected to occur in the ambient environment. Likewise, the cylindrical particulates present on the anodized region may consist of unreacted Si that is rendered free via generalized corrosion. For example, the particulates may consist of "crystallites" of Si seen to be present near the surface of corroded microtensile specimens.[1] As the cylindrical particles were solely present within the anodized region, they are thought to be related to the galvanic corrosion process. Regardless, the compositional analysis suggests that no new chemical species have been accumulated at the surface of corroded Si.

Conclusions

To support the previous study of galvanic corrosion using microtensile specimens, a collective study consisting of morphological, resistive probe, sessile drop, and electrochemical characterizations was utilized to identify key parameters of influence, such as the type of Si or the composition of the etchant. Important results and the associated conclusions are summarized as follows: The measured porosity for corroded Si ranged from 20 to 47%, but was estimated in some cases to exceed 70%. Both the porosity and thickness were found to vary according to the amount (surface area) of metal present. Pores present on Si etched in UDHF:H_2O but with no metal present demonstrate the greater activity associated with the additional hydroxide ions present in that etchant. The porosity, taken as 50%, allows corrosion current density or depth of damage to be estimated according to Faraday's law.

Resistive probe structures indicated that corrosion current asymptotically decreases over time for all specimens and etchants examined. For polySi, resistive probe structures identified an acceleration factor (2× for Poly-0 and 4× for Poly-1) for UDHF and UDHF:H_2O, attributed to microstructure specific attack. The difference between etchants was not as obvious for SOI resistive probe structures, based on the proportionally smaller amount of area consumed and their lack of microstructural defects. Corrosion current was found to vary exponentially with the amount of metal present, implying current is limited by the surface area of the cathode. Lastly, the degradation of polySi was found to exhibit three behavior regimes, including (*i*) rapid initiation related to the formation of a porous surface layer, (*ii*) steady-state corrosion bearing characteristics motivated by the surface wetting of the etchant utilized, and (*iii*) sudden catastrophic failure associated with grain boundary attack.

The difference in electrochemical potential between Au and Si was measured to be 0.90 V, indicating that the oxidation of Si is thermodynamically favored in HF. From the measured etch rate of MEMS structures, the corrosion current density was found to range between 0.008 and 0.55 mA/cm^2, with the value of 0.25 mA/cm^2 being considered to be a conservative estimate in most cases. The substantial current observed in polarization curves far exceeds this current estimate, identifying that the galvanic corrosion process is current limited for micromachined Si and operates within the PS formation regime. Electrochemical characterization indicated that the use of illumination was not significant for the degenerately-doped SOI and polySi layers, whereas a less-doped (100) SCS was strongly limited by light. Polarization curves revealed improved speed and greater current density when the Triton-X was added to UDHF, corresponding to the greater effective surface area at the anode enabled by the superior surface wetting of the surfactant, which readily wets to both Si and PS. Triton-X was additionally found to result in a more uniform, stable response attributed to the removal of hydrogen bubbles during applied current conditions, indicating it may be used to regulate corrosion damage. UDHF:H_2O demonstrated decreased speed and was typically the last etchant to stabilize over time. This behavior is attributed to the evolution of surface coverage over time as well as the greater viscosity for UDHF:H_2O. In particular, the poor surface wetting for this etchant should initially result in microstructure specific attack that later becomes more broadly distributed as the enhanced activity associated with additional hydroxide ions is realized. In electrochemical characterization, the similar behavior observed between the SOI and polySi materials suggests that the physiochemistry (surface wetting characteristics of the etchant) is among the most significant factors affecting the corrosion of Si. The surface wetting characteristics, which were slightly improved for polySi by its roughness, were formally quantified using the sessile drop characterization. The lack of overt damage for the chronopotentiometry specimens further reiterates that corrosion in micromachined Si occurs via PS formation and further implies catastrophic failure occurs at grain boundaries for UDHF and UDHF:H_2O. Lastly, cylindrical and spherical particulates uniquely observed at the surface of corroded Si are thought to consist of Si or O rendered mobile by HF.

Acknowledgments

The authors acknowledge Bonnie McKenzie and Mike Rye of Sandia National Laboratories for their help with microscopy and specimen preparation, Terry Guilinger, Michael J. Kelly, and Kevin Zavadil of Sandia National Laboratories for their help with fixturing and initial investigations, and Professor Carl Koval of the Chemistry Department at the University of Colorado for his mentoring and advice during electrochemical characterization. The authors also thank Narayan Doddapaneni, from PowerCell Technologies, for discussions and equipment for characterizing the Cu/CuF reference electrode. This material is based on work supported, in part, by the U.S. Army Research Laboratory and the U.S. Army Research Office under grant no. W911NF-06-1-0342. Portions of the study were performed at the Nano Characterization Facility at the University of Colorado at Boulder.

University of Colorado assisted in meeting the publication costs of this article.

References

1. D. C. Miller, B. L. Boyce, P. G. Kotula, and C. R. Stoldt, *J. Appl. Phys.*, **103**, 123518 (2008).
2. C. M. A. Ashruf, P. J. French, P. M. M. C. Bressers, and J. J. Kelly, *Sens. Actuators, A*, **74**, 118 (1999).
3. X. Xia, C. Ashruf, P. French, and J. Kelly, *Chem. Mater.*, **12**, 1671 (2000).
4. A. Splinter, J. Stürmann, and W. Benecke, *Proc. SPIE*, **4174**, 398 (2000).
5. O. N. Pierron and D. D. Macdonald, and C. L. Muhlstein, *Appl. Phys. Lett.*, **78**, 211919 (2005).
6. M. Huh, Y. Yu, H. Kahn, J. H. Payer, and A. H. Heuer, *J. Electrochem. Soc.*, **153**, G644 (2006).
7. H. Kahn, C. Deeb, I. Chasiotis, and A. H. Heuer, *J. Microelectromech. Syst.*, **14**, 914 (2005).
8. O. Bisi, S. Ossicini, and L. Pavesi, *Surf. Sci. Rep.*, **38**, 1 (2000).
9. J. C. Vial and J. Derrien, *Porous Silicon Science and Technology*, Springer-Verlag, Berlin (1995).
10. L. T. Canham, *Properties of Porous Silicon*, IEEE, New York (1997).
11. X. G. Zhang, *Electrochemistry of Silicon and Its Oxide*, Kluwer, Dordrecht (2001).
12. D. C. Miller, W. L. Hughes, Z.-L. Wang, K. Gall, and C. R. Stoldt, *J. Microelectromech. Syst.*, **16**, 87 (2007).
13. I. Chasiotis and W. G. Knauss, in *Comprehensive Structural Integrity*, Vol. 8, Elsevier, New York (2003).
14. P. Guyander, P. Joubert, M. Guendouz, C. Beau, and M. Sarrett, *Appl. Phys. Lett.*, **65**, 1787 (1994).
15. D. A. Jones, *Principles and Prevention of Corrosion*, 2nd ed., Prentice-Hall, Englewood Cliffs, NJ (1996).
16. R. C. Anderson, R. S. Muller, and C. W. Tobias, *J. Electrochem. Soc.*, **138**, 3406 (1991).
17. R. Irwin, W. Zhang, K. Harsh, and Y. C. Lee, *Proc. IEEE*, 293 (1998).
18. M. J. Madou, *Fundamentals of Microfabrication the Science of Miniaturization*, 2nd ed., CRC Press, Boca Raton (2002).
19. V. Lehmann and U. Gösele, *Appl. Phys. Lett.*, **58**, 856 (1991).
20. D. Gräf, M. Grunder, and R. Schultz, *J. Vac. Sci. Technol. A*, **7**, 808 (1989).
21. K. Miller, A. Cowen, G. Hames, and B. Hardy, *SOIMUMPS Design Handbook*, Rev. 4, MEMSCAP, Inc., Research Triangle Park (2005).
22. J. Carter, A. Cowen, B. Hardy, R. Mahadevan, M. Stonefield, and S. Wilcenski, *Poly-MUMPs Design Handbook*, Rev. 11, MEMSCAP, Inc., Research Triangle Park (2005).
23. D. C. Miller, B. L. Boyce, M. T. Dugger, T. E. Buchheit, and K. Gall, *Sens. Actuators, A*, **138**, 130 (2007).
24. M. G. Buehler, S. D. Grant, and W. R. Thurber, *J. Electrochem. Soc.*, **125**, 650 (1978).
25. L. J. van der Pauw, *Philips Res. Rep.*, **13**, 1 (1958).
26. K. Inaba, *Anal. Sci.*, **17**, 349 (2001).
27. R. L. Higginson and C. M. Sellars, *Worked Examples in Quantitative Metallography*, Maney, London (2003).
28. F. M. Fowkes, *Contact Angle, Wettability, and Adhesion*, American Chemical Society, Washington (1964).
29. W. D. Kingery, H. K. Bowen, and D. R. Uhlman, *Introduction to Ceramics*, 2nd ed., John Wiley & Sons, Hoboken, NJ (1976).
30. D. C. Miller, Ph.D. Thesis, University of Colorado, Boulder (2007).
31. G. Willeke and K. Kellerman, *Semicond. Sci. Technol.*, **11**, 415 (1996).
32. C. C. Chang, A. C. Adams, G. Quintana, and T. T. Sheng, *J. Appl. Phys.*, **45**, 252 (1974).
33. J. S. Johannessen, W. E. Spicer, J. F. Gibbons, and J. D. Plummer, *J. Appl. Phys.*, **49**, 4453 (1978).
34. T. Kimura, M. Hirose, and Y. Osaka, *J. Appl. Phys.*, **56**, 932 (1984).
35. Y. Mizokawa, W. B. Ying, Y. B. Yu, Y. Kamiura, M. Iida, and K. Kawamoto, *Appl. Surf. Sci.*, **100**, 561 (1996).
36. W. B. Ying, Y. Mizokawa, Y. Kamiura, K. Kawamoto, and W. Y. Yang, *Appl. Surf. Sci.*, **181**, 1 (2001).
37. P. J. Hesketh, C. Ju, S. Gowda, E. Zanoria, and S. Danlyuk, *J. Electrochem. Soc.*, **140**, 1080 (1993).
38. A. W. Adamson, *Physical Chemistry of Surfaces*, 5th ed., John Wiley & Sons, Hoboken, NJ (1990).
39. U. Roth, O. Paulus, and U. Menyes, *Colloid Polym. Sci.*, **273**, 800 (1995).
40. D. R. Turner, *J. Electrochem. Soc.*, **105**, 402 (1958).
41. D. R. Lide, *Handbook of Chemistry and Physics*, 87th ed., CRC, Boca Raton (2006).
42. K. W. Kolasinski, *Phys. Chem. Chem. Phys.*, **5**, 1270 (2003).
43. B. Burrows, *J. Electrochem. Soc.*, **115**, 348 (1968).
44. G. G. Totir, G. S. Chottiner, C. L. Gross, and D. A. Scherson, *J. Electroanal. Chem.*, **532**, 151 (2002).
45. G. L. Pearson and J. Bardeen, *Phys. Rev.*, **75**, 865 (1949).
46. R. F. Pierrot, *Advanced Semiconductor Materials*, Vol. XI, Addison-Wesley, Reading (1987).
47. M. Houston, R. T. Howe, and R. Maboudian, *J. Appl. Phys.*, **81**, 3474 (1997).